Accurate ionization thresholds of atoms subject to half-cycle pulses

S. Yoshida, C. O. Reinhold, and J. Burgdörfer*
Physics Division, Oak Ridge National Laboratory, Oak Ridge, Tennessee 37831-6373
and University of Tennessee, Knoxville, Tennessee 37996-1200

B. E. Tannian, R. A. Popple, and F. B. Dunning
Department of Physics and the Rice Quantum Institute, Rice University, P.O. Box 1892, Houston, Texas 77251
(Received 18 December 1997)

The evolution of Rydberg states of hydrogen and alkali-metal atoms subject to short half-cycle pulses is studied. The convergence of the numerical solutions of the time-dependent Schrödinger equation based on an expansion of the electronic wave function in a finite basis set of Sturmian functions is analyzed in detail. It is shown that the accuracy of such calculations can be established by investigating the stabilization of the transition probabilities with respect to the parameters that define the basis set. The dependence of the quantum and classical ionization thresholds on the pulse shape is investigated. The calculations are compared with experimental data for various pulse profiles, which feature slow or fast rise times. The results show that the ionization thresholds for long pulses are very sensitive to the rise time of the electric field.
[S1050-2947(98)00309-6]

PACS number(s): 32.80.Rm, 02.60.−x

I. INTRODUCTION

During the last few years, the ionization and excitation of Rydberg atoms by pulsed unidirectional electric fields, termed half-cycle pulses (HCPs), have been investigated extensively. Experiments have reached the regime in which the effective duration of the pulses T_p and the peak fields F_p are of the order of the classical electron orbital period $T_{n_i} = 2\pi n_i^3$ and the Coulomb electric field $F_{n_i} = n_i^{-4}$ in the atom, respectively (where n_i is the initial principal quantum number of the Rydberg atom and atomic units are used throughout) [1–5]. This has been accomplished, for example, by using subpicosecond pulses and relatively low Rydberg levels ($n_i \sim 30$) [1] or, alternatively, by using nanosecond pulses and very-high-n states ($n_i \sim 400$) [3].

The experimental advances have stimulated a large number of theoretical investigations using quantum and classical approaches [6–10]. In exploring the dynamics of Rydberg states, classical scaling invariances have proven to be a very useful tool [11]. Suppose that a pulse $F(t)$ interacts with a Rydberg atom with quantum numbers n_i, l_i, m during an effective period of time T_p. For a given pulse shape, classical scaling laws imply that transition probabilities are a function of only the scaled variables $L_0 = l_i/n_i$, $m_0 = m/n_i$, $F_0 = F_p/F_{n_i}$, and $T_0 = T_p/T_{n_i}$. Thus, deviation from classical scaling invariances provides a signature of nonclassical dynamics. For typical experimental conditions where $L_0 \ll 1$ and $|m_0| \ll 1$, it has been found that the threshold fields for ionization F_0^{thr}, expressed as a function of T_0, lie on a universal, classical scaling invariant curve connecting the adiabatic ($T_0 \gg 1$) and sudden regimes ($T_0 \ll 1$). For long duration pulses, ionization results primarily from the escape over the potential barrier, generated by the atomic and applied fields, whose height is determined by the value of F_0. The threshold field for such ionization is proportional to n_i^{-4}. In contrast, application of a very short electric-field pulse with duration $T_0 \ll 1$ lowers the Coulomb barrier only momentarily. Ionization can still occur, however, if the impulse delivered to the excited electron by the pulsed field $\Delta p = -\int F(t)dt$ is sufficient to increase its energy by an amount that is greater than its original binding energy. Consequently, the electric-field dependence of the ionization threshold crosses over from the n_i^{-4} scaling characteristic of the adiabatic limit to a n_i^{-1} scaling in the sudden, ultrashort pulse, $T_0 \ll 1$ limit. Recent experimental studies have succeeded in employing short HCPs to examine the time evolution of the momentum of the electron associated with the development of coherent atomic wave packets [12–14].

The first ionization thresholds measured experimentally using short HCPs [1] were found to disagree with classical and quantum scaling invariant results [15], raising questions as to the validity of the theory. However, it was subsequently found [2] that this disagreement resulted from difficulties in both the calibration of experimental peak fields and in the determination of the pulse shape. More recently, the scaling invariant results were found to be in excellent agreement with the experimental measurement of Frey *et al.* [3] undertaken at very high $n_i \sim 400 \sim 500$. The use of such values of n_i offers the advantage that the ultrashort pulse regime can be examined using pulses of a few nanoseconds in duration, which can be readily generated and accurately measured. However, new experiments by Kristensen *et al.* [4] using long pulses with $T_0 \gtrsim 4$ suggest departures from the scaling invariant results. In the following, we show that this can, at least in part, be explained by the fact that in the long pulse regime the threshold ionization fields depend quite sensitively on the exact shape of the HCPs, particularly on their rise times.

*Present address: Institute for Theoretical Physics, Technical University of Vienna, A-1040 Vienna, Austria.

Here we present a comprehensive description of our quantum calculations, the results of which have been briefly discussed in earlier publications [6–8]. These calculations employ an expansion of the electronic wave function using a finite Sturmian basis set. The main focus of this paper is on the extension of theory to longer duration pulses where convergence with respect to basis size becomes an increasingly critical issue. In order to establish convergence we apply the method of stabilization. The stabilization method has been well-established for time-independent problems, in particular for the calculation of the position and width of resonances [16]. Also, early accurate calculations of scattering phase shifts in e-H collisions [17] used the stability of the result with respect to a control parameter in the basis to verify the accuracy of the compared phase shifts. In the following, we discuss the application of this method to the solution of an explicitly time-dependent Schrödinger equation. Here, the stability of transition amplitudes is required. Because of the implicit dependence on the different sectors of Hilbert space, in which the initial and final states reside, stability must be established on a state-to-state basis for each transition and cannot be expected to hold globally.

We show that the stability analysis with respect to the Sturmian parameter provides a good test for the convergence and accuracy of the solutions with a finite basis size. As an application, we extend our previous calculations to longer pulse lengths and consider various pulse shapes. We discuss the correspondence between classical and quantum-mechanical results and we present experimental data that corroborate the calculations. A brief description of our classical approach is included in the Appendix. The present data are able to resolve, at least partially, the issue of the apparent breakdown of scaling invariance reported by Kristensen *et al.* [4].

II. PROBLEM

We shall be concerned with time evolution of an electron in an atom with Hamiltonian H_{at}, which is subject to a time-dependent perturbation $V(t)$ during the interval $0<t<T$. The dynamics of the electron is governed by the time-dependent Hamiltonian

$$H(t)=H_{at}+V(t)=H_{at}+zF(t), \tag{1}$$

$$H_{at}=\frac{p^2}{2}+V_{at}(r), \tag{2}$$

where $\boldsymbol{r}=(x,y,z)$ and $\boldsymbol{p}$ are the position and momentum of the electron, respectively, and $F(t)$ is a time-dependent electric field whose direction defines the positive z axis. For hydrogen, $V_{at}=-1/r$. For alkali-metal atoms A, the interaction of the electron with the core A^+, can be represented in terms of a parametrized model potential that yields accurate quantum defects and satisfies the correct boundary conditions at small ($V_{at}\rightarrow -Z/r$, Z being the nuclear charge) and large distances ($V_{at}\rightarrow -1/r$). Clearly, electron-correlation effects are neglected in this approach.

The time evolution of the wave function $|\Psi(t)\rangle$ of the electron is governed by the Schrödinger equation

$$i\frac{\partial|\Psi(t)\rangle}{\partial t}=H(t)|\Psi(t)\rangle \tag{3}$$

with the boundary condition

$$|\Psi(t)\rangle \underset{t\rightarrow 0}{\rightarrow} |\varphi_i\rangle. \tag{4}$$

The transition probability from this initial state φ_i to a final state φ_f at $t=T$ is given by

$$P_{i,f}(T)=|\langle\varphi_f|\Psi(T)\rangle|^2=|\langle\varphi_f|U(T,0)|\varphi_i\rangle|^2, \tag{5}$$

where $U(T,0)$ is the time evolution operator. By analyzing the effects of pulse shape, we characterize the pulse by three parameters: a peak field F_p, a full-width half-maximum duration T_p, and a momentum transfer $\Delta p=-\int_0^T dt\ F(t)$. In the limit of ultrashort pulses, the sudden approximation yields

$$U(T,0) \underset{T\rightarrow 0}{\rightarrow} \exp(iz\ \Delta p). \tag{6}$$

In this limit only the momentum transfer Δp enters. However, with increasing pulse duration the ionization process also becomes a function of F_p and T_p. We analyze the effects of pulse shape by introducing the following prototype shape functions: (a) a rectangular pulse,

$$F(t)=F_p, \quad T_p=T, \quad \Delta p=-F_pT_p; \tag{7}$$

(b) a triangular pulse,

$$F\left(t<\frac{T}{2}\right)=2F_p\frac{t}{T}, \quad F\left(t>\frac{T}{2}\right)=2F_p\left(1-\frac{t}{T}\right),$$

$$T_p=\frac{T}{2}, \quad \Delta p=-F_pT_p; \tag{8}$$

(c) a Gaussian pulse,

$$F(t)=F_p\exp\left[\frac{[t-(T/2)]^2}{\sigma^2}\right], \quad T=5.01\sigma, \quad T_p=1.67\sigma,$$

$$\Delta p=-1.06F_pT_p; \tag{9}$$

and (d) various experimental nanosecond pulse shapes that model the sudden rise time of (a) and the slow rise time of (b). We note that the idealized pulse-shape functions (a), (b), and (c) can only be approximately realized experimentally. While for the present experiments with nanosecond pulses, the pulse shape can be accurately measured, reliable pulses in the subpicosecond range have proven to be more difficult.

In order to compare transition amplitudes with different initial quantum levels n_i, we display results in terms of scaled variables:

$$F_0=F_p/F_{n_i}=n_i^4F_p, \quad T_0=T_p/T_{n_i}=T_p/(2\pi n_i^3),$$

$$\Delta p_0=\Delta p/p_{n_i}=n_i\Delta p, \tag{10}$$

where F_{n_i}, T_{n_i}, and p_{n_i} are the average electric field, classical orbital period, and momentum associated with the initial state of the electron.

A. Sturmian basis set

Suppose that $\{|\phi_k^\lambda\rangle,\ k=1,2,\ldots,\infty\}$ is a complete basis set of orthonormal wave functions, which depends on a parameter λ (i.e., each value of λ provides a different complete set). The Schrödinger equation can be solved using an expansion of the wave function

$$|\Psi(t)\rangle=\sum_{k=1}^{N_{max}} a_k(t)|\phi_k^\lambda\rangle, \tag{11}$$

which transforms Eq. (3) into an infinite set of coupled equations ($N_{max}=\infty$) for the expansion coefficients

$$i\frac{da_k(t)}{dt}=\sum_{j=1}^{N_{max}}\langle\phi_k^\lambda|H|\phi_j^\lambda\rangle a_j(t). \tag{12}$$

In practice, only a finite number of coupled equations can be solved simultaneously and, therefore, the basis must be truncated; i.e., N_{max} is finite.

Our orthonormal basis set is constructed from a nonorthonormal Sturmian basis set [18–21], which is defined by the complete set of functions obeying

$$\left(\frac{p^2}{2}-\frac{n\lambda}{r}\right)|\psi^\lambda\rangle=-\frac{\lambda^2}{2}|\psi^\lambda\rangle, \tag{13}$$

where $n=1,2,\ldots,\infty$, and the parameter λ defining the set is called the Sturmian parameter. In general, this parameter can be taken to be a complex number [20,21]. In this paper, we assume that λ is a positive real number. Note that Eq. (13) is identical to the eigenvalue equation for a hydrogenic atom in a quantum level n for an effective nuclear charge $Z_{eff}=n\lambda$. Thus, this equation can easily be solved using standard methods for separation of the variables in either spherical [$r=\sqrt{x^2+y^2+z^2}$, $\theta=\cos^{-1}(z/r)$, $\phi=\tan^{-1}(y/x)$] or parabolic ($\xi=r+z$, $\eta=r-z$) coordinates. The solutions of Eq. (13), in spherical and parabolic coordinates, are given by

$$\langle\boldsymbol{r}|\chi_{n,l,m}^\lambda\rangle=\frac{2}{\sqrt{n}}\lambda^{3/2}\left(\frac{(n-l-1)!}{(n+l)!}\right)^{1/2}(2r\lambda)^l \times e^{-\lambda r}L_{n-l-1}^{2l+1}(2\lambda r)Y_l^m(\theta,\phi), \tag{14}$$

$$\langle\boldsymbol{r}|\chi_{n_1,n_2,m}^\lambda\rangle=\frac{e^{m\phi}}{\sqrt{\pi n}}\left(\frac{n_1!n_2!}{(n_1+m)!(n_2+m)!}\right)^{1/2} \times\lambda^{(m+3/2)}e^{-\lambda/2(\xi+\eta)}(\xi\eta)^{m/2}L_{n_1}^m(\lambda\xi) \times L_{n_2}^m(\lambda\eta), \tag{15}$$

where n, l, and m are spherical quantum numbers, n_1, n_2, and m are parabolic quantum numbers [$n=n_1+n_2+m+1$, $n_{1,2}=0,1,\ldots,(n-|m|-1)$], L_n^m denotes a Laguerre polynomial, and Y_l^m is a spherical harmonic. In Eq. (15), $m\geqslant 0$ is assumed. For negative m, we have $\langle\boldsymbol{r}|\chi_{n_1,n_2,m}^\lambda\rangle=(-1)^m\langle\boldsymbol{r}|\chi_{n_1,n_2,-m}^\lambda\rangle^*$. A complete and countable basis set for the full Hilbert space is generated by changing n, l, and m (or n_1, n_2, and m). Because the Hamiltonian in Eq. (1) has cylindrical symmetry, m is a constant of motion. In practice, we use $1\leqslant n\leqslant n_{max}$, which, for $m=0$, corresponds to a number of states $N_{max}=n_{max}(n_{max}+1)/2$.

Since Sturmian functions are not orthogonal, we define the basis set $\{|\phi_k^\lambda\rangle,\ k=1,2,\ldots,N_{max}\}$, entering Eq. (11), as the set of orthonormal eigenvalues of the finite Sturmian representation of H_{at}. Namely,

$$|\phi_k^\lambda\rangle=\sum_{i=1}^{N_{max}} b_i^k|\chi_{n_i,l_i,m}^\lambda\rangle, \tag{16}$$

$$\hat{H}_{at}\hat{b}^k=E_k\hat{S}\hat{b}^k, \tag{17}$$

where E_k is the eigenenergy of an electron in the state $|\phi_k^\lambda\rangle$, $\hat{S}$ is the overlap matrix ($S_{ij}=\langle\chi_{n_i,l_i,m}|\chi_{n_j,l_j,m}\rangle$), and $\hat{b}^k$ and $\hat{H}_{at}$ are the column vector and matrix representation of $|\phi_k^\lambda\rangle$ and H_{at} in the Sturmian basis set, respectively. Using the orthonormal basis set that diagonalizes $\hat{H}_{at}$ greatly simplifies the evaluation of physical transition probabilities. For example, the ionization probability at $t=T$ is simply given by

$$P_{ion}(T)=1-\sum_{E_k\leqslant 0}|\langle\phi_k^\lambda|\Psi(T)\rangle|^2. \tag{18}$$

By definition, a bound hydrogenic state can be written as $|n,l,m\rangle=|\chi_{n,l,m}^\lambda\rangle$ if $\lambda=Z/n$. For this reason, it is convenient to introduce the alternative Sturmian parameter $n_s=1/\lambda$. For hydrogen ($V_{at}=-1/r$) the value of n_s determines whether a given n shell is exactly reproduced by the basis (i.e., when $n_s=n$). In general, n_s takes a real value. Understanding which other physical energy levels can be properly described within a finite basis requires additional analysis.

Figure 1 shows the norm of the projection of a hydrogenic bound state on a finite subspace,

$$\sum_{k=1}^{N_{max}}|\langle n_1,n_2,m|\phi_k^\lambda\rangle|^2, \tag{19}$$

for different values of n_s and n_{max}. A basis set that provides a good representation of the bound state should yield a norm very close to unity. This is an obvious prerequisite for calculating the evolution in the presence of the field. As expected, the norm becomes closer to unity for a larger range of n levels, as the basis size increases. Note, however, that the n levels, which are well represented, strongly depend on the value of n_s. High n levels are clearly described better using higher values of n_s (here $n_s=10$) rather than the lower value (here $n_s=1$) and vice versa. Since both basis sets contain the same number of states, this indicates that the basis with the lower value of n_s involves a larger number of continuum states ($E_k>0$) and, hence, provides a more suitable representation of the continuum.

Because Sturmian functions decay exponentially in the limit $r\to\infty$ [see Eq. (15)], continuum states cannot be exactly reproduced. It is, however, possible to find a good representation of continuum wave functions in a limited range

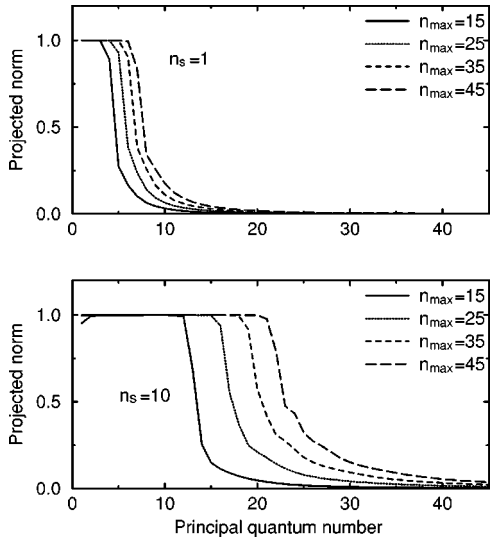

FIG. 1. Norm of the projection of a hydrogenic state with $n_1=m=0$ onto different Sturmian basis sets as a function of the principal quantum number of the hydrogenic state. The different Sturmian basis sets are characterized by $n_{max}=15,25,35,45$ and $n_s=1$ or $n_s=10$.

$r \lesssim R$, which is proportional to the maximum average radius of a Sturmian function with $n=n_{max}$, i.e., $R \propto r_{max}=n_s n_{max}$. An accurate solution of the Schrödinger equation can be obtained as long as the wave function is localized in this region of coordinate space. Figure 2 shows a comparison

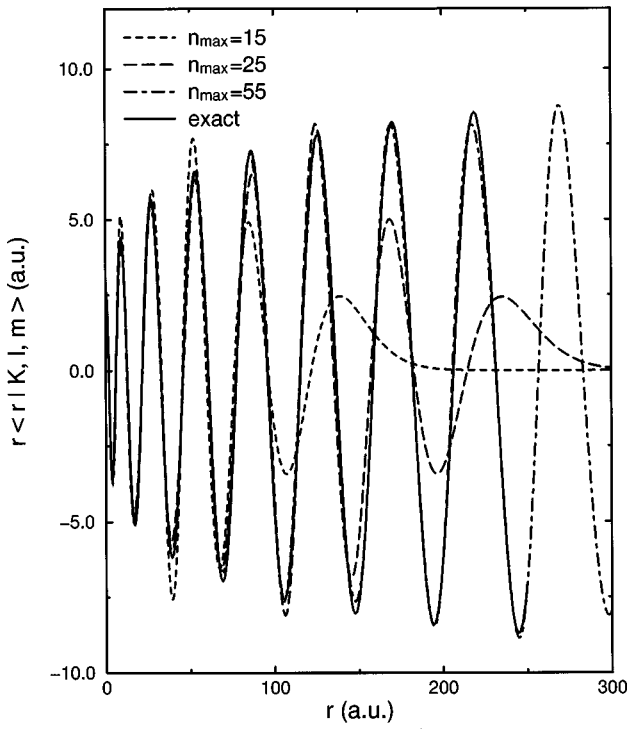

FIG. 2. Comparison of the exact and approximate continuum wave function times the radius using different basis sizes for a spherical continuum state with $E=0.0032$ a.u., $l=m=0$. The Sturmian parameter for the Sturmian functions has been chosen to be $n_s=5$ and all of the wave functions are normalized to the same value at the first minimum.

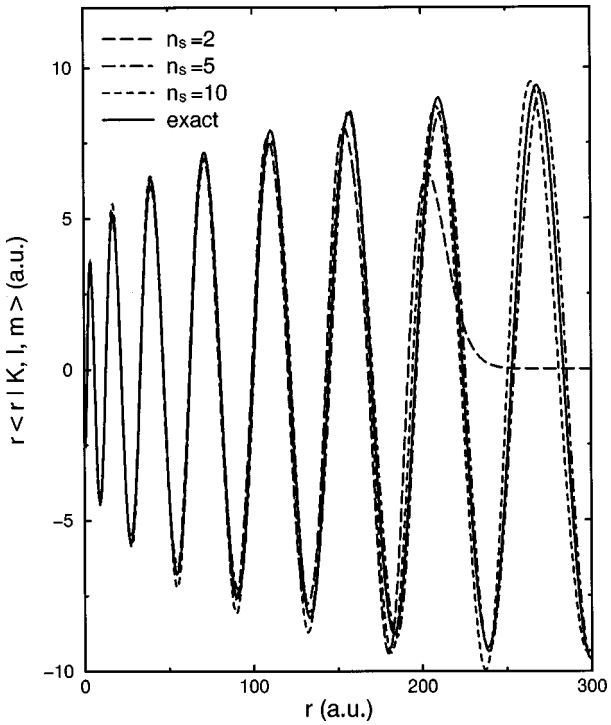

FIG. 3. Comparison of the exact and approximate continuum wave function times the radius using various Sturmian parameters n_s for a spherical continuum state with $E=0.0016$ a.u., $l=m=0$. The finite basis size is $N_{max}=1540$ (i.e., $n_{max}=55$) and all of the wave functions are normalized to the same value at the first minimum.

of a spherical continuum state calculated from a finite Sturmian basis set with the exact continuum state given by

$$\langle \boldsymbol{r}|K,l,m\rangle = \sqrt{\frac{2}{\pi}} e^{\pi(\eta/2)} \frac{|\Gamma(1+l+i\eta)|}{(2l+1)!} (2Kr)^l e^{-iKr} \times {}_1F_1[1+l+i\eta, 2l+2, 2iKr] Y_l^m(\theta,\phi), \tag{20}$$

where $\eta=Z/K$ and ${}_1F_1$ is a confluent hypergeometric function. The wave function in the figure has an energy $E=K^2/2=0.0032$ a.u., $m=0$, and $l=0$. The approximate wave functions have been calculated using $n_s=5$ and, therefore, $r_{max}=75,125,225,275$ a.u. for $n_{max}=15,25,45,55$, respectively, which contains the range of r values in the figure. The larger the basis size, the larger the range of radii for which the approximate wave function agrees with the exact one. Note that the precise radius up to which a basis set can reproduce a continuum state is a function of not only r_{max} but also the wave number K. The maximum wave vector that can be represented properly in a finite Sturmian basis is proportional to $\sim n_s^{-1}$. This is illustrated in Fig. 3, which shows a spherical continuum state with $E=0.0016$ a.u., $l=m=0$, obtained as the Sturmian parameter is changed while maintaining the basis size fixed. As expected, the smaller the n_s, the better the agreement between the approximate and the exact wave functions. Thus, a finite Sturmian basis set can approximate continuum wave functions within certain ranges of both wave number and radius, which depend on n_s and n_{max}.

B. Numerical solution of the time-dependent Schrödinger equation

Instead of directly solving the set of coupled equations in Eq. (12), the Schrödinger equation (3) is integrated using a more efficient approach usually called the split operator method [22]. Briefly, the time evolution operator from $t=0$ to $t=T$ is broken down into a product of N evolution operators for time intervals $\delta t = T/N = t_{k+1} - t_k$,

$$U(T,0) = \prod_{k=0}^{N-1} U(t_{k+1}, t_k), \tag{21}$$

where $t_0 = 0$ and $t_N = T$. In each step the evolution operator is split at the midpoint

$$U(t_{k+1}, t_k) \simeq \exp\left(-\frac{i}{2} H_{at} \delta t \right) \exp(iz\,\delta p_k) \exp\left(-\frac{i}{2} H_{at} \delta t \right), \tag{22}$$

$$\delta p_k = -\int_{t_k}^{t_{k+1}} F(t)\, dt, \tag{23}$$

which has an $O((\delta t)^3)$ error. The error arises from the fact that the commutators $[H_{at}, z] \neq 0$ and, in general, $[H(t), H(t')] \neq 0$. The resulting evolution operator becomes

$$U(T,0) = \exp\left(-\frac{i}{2} H_{at} \delta t \right) \left[\prod_{k=0}^{N-1} \exp(iz\,\delta p_k) \exp(-iH_{at}\delta t) \right] \times \exp\left(\frac{i}{2} H_{at} \delta t \right), \tag{24}$$

which contains simpler operators of the form $\exp(-iH_{at}\delta t)$, representing a free evolution, and $\exp(iz\delta p_k)$, representing the effect of the perturbation. The latter is equivalent to delivering a momentum transfer (or boost) δp_k to the electron.

In order to calculate the time evolution of the wave function, the operators $\exp(-iH_{at}\delta t)$ and $\exp(iz\delta p_k)$ are replaced by their unitary matrix representations within the basis set, $\exp(-i\hat{H}_{at}\delta t)$ and $\exp(i\hat{z}\delta p_k)$, respectively, where $\hat{A}$ denotes a finite matrix representation of the operator A in our orthonormal basis. Since our basis set diagonalizes $\hat{H}_{at}$, $\exp(-i\,\hat{H}_{at}\delta t)$ is also diagonal with matrix elements $\exp(-i\,E_k\delta t)$ $k=1,2,\ldots,N_{max}$. The boost matrix $\exp(i\hat{z}\delta p_k)$ can be evaluated using a unitary transformation

$$\exp(i\hat{z}\,\delta p_k) = \hat{O}_z \exp(-i\hat{D}_z \delta p_k)\ \hat{O}_z^t, \tag{25}$$

where $\hat{O}_z$ is a unitary matrix that diagonalizes the dipole matrix $\hat{z}$, and $\hat{D}_z$ is a diagonal matrix whose elements are the eigenvalues of the dipole matrix. Finally, the vector containing the expansion coefficients of the wave function Eq. (11) is given by $\hat{a}(T) = \hat{U}(T,0)\hat{a}(0)$.

For a rectangular pulse [Eq. (7)], the evolution operator $\hat{U}(T,0) = \exp[-i(\hat{H}_{at} + \hat{z}F_p)T]$ can be calculated by diagonalization, since, in this case, the total Hamiltonian is time-independent between 0 and T. Therefore, the numerical error of the split operator method associated with the multiplication of many large matrices can be checked by comparing

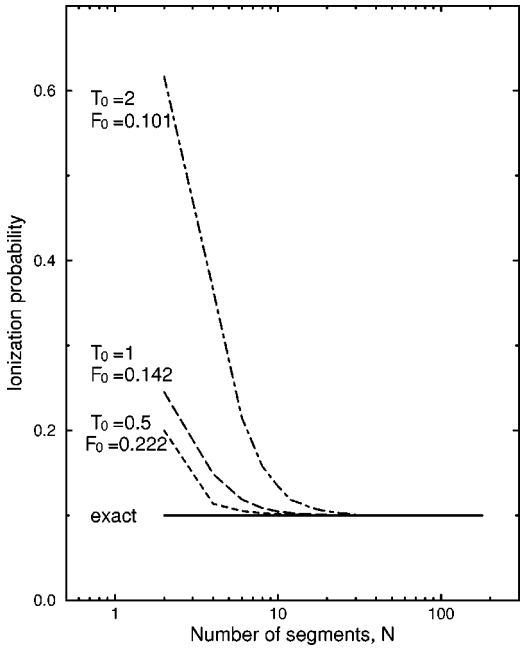

FIG. 4. Probability of ionization of H($n_1=4$, $n_2=0$, $m=0$) atoms by rectangular HCPs of various scaled durations T_0 as a function of the number of splits of the evolution operator. For each value of T_0 the scaled field strengths F_0 have been chosen such that the ionization probability is 10%. The basis size is set to $N_{max} = 1035$ (i.e., $n_{max} = 45$) and the Sturmian parameter to $n_s = 5$.

results from the split operator method with the exact one from full evolution operator diagonalization. Figure 4 illustrates the convergence of the split operator method for different scaled durations as a function of the number of splits N of the evolution operator. Clearly, the longer the pulse, the larger the number of splits required to reach convergence. For short HCPs, convergence is reached after about ten splits per classical orbital period (i.e., see the result for $T_0 = 1$).

III. THE STABILIZATION METHOD

Since the number of basis states N_{max} is finite, two important questions arise: (i) how large should the basis set be in order to obtain an accurate result, and (ii) what value should the Sturmian parameter have in order to get an accurate result with the smallest basis set.

In order to answer these questions we apply the so-called stabilization method to the time-dependent Schrödinger equation. The time-dependent stabilization method can be viewed as an extension of the time-dependent variational principle, very much like the case of the stationary Schrödinger equation [16]. While the variational principle assures that the solution of the form [Eq. (12)] is an exact result within the given basis size, the stabilization method goes beyond that by providing information as to how accurate the solution is within the whole Hilbert space. The standard form of stabilization is associated with the convergence of a given transition probability $P_{i,f}$ with respect to the basis size N_{max} (in the limit $N_{max} \to \infty$, $P_{i,f}$ stabilizes).

A more useful stabilization property exists with respect to the parameter λ, which defines the basis set for a fixed value of N_{max}. This fact can be understood using the schematic picture in Fig. 5. Suppose that the full Hilbert space is rep-

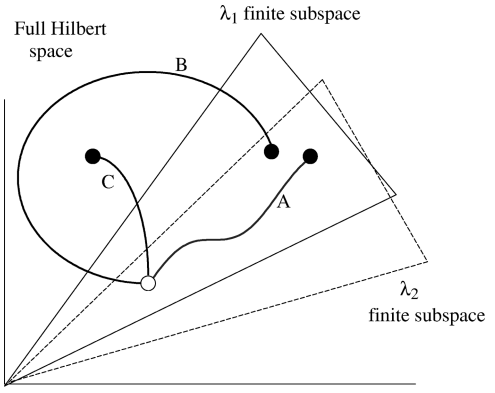

FIG. 5. Schematic picture of the full Hilbert space. The trajectories A, B, and C represent different exact solutions of the time-dependent Schrödinger equation starting from the same initial state (represented by an open circle) but with different final wave functions (represented by solid circles). The triangular regions denote two finite Hilbert spaces. See text.

resented by the plane such that the ''exact'' evolution of the wave function is given by a trajectory in the plane (e.g., trajectories A, B, and C). Two finite Hilbert subspaces, generated by bases with parameters λ_1 and λ_2, are represented in the figure by triangular regions. These regions can be chosen to provide a good representation of the initial wave function (open circle) but may not always contain the exact final wave function (solid circles). If a trajectory such as A is contained in the overlap of both triangular regions, the calculation of the evolution of the wave function should be stable with respect to a change from λ_1 to λ_2, i.e., the solution should be ''exact.'' In turn, if a trajectory such as B or C leaves the finite subspaces subtended, the approximate calculations in each basis set will yield, in general, different nonconverged results. There could be, of course, rare exceptions such that convergence is reached (not necessarily to the correct limit) even if trajectories corresponding to these results leave the finite subspace. Thus, an accurate calculation of a transition probability should be stable with respect to variations of the basis set, i.e., λ. Note, however, that stabilization of a given transition probability does not imply stabilization for other transition probabilities (i.e., some trajectories may leave the domain subtended).

Figure 6 demonstrates the applicability of the stabilization method for calculating the ionization probability for hydrogen atoms in the $|n_1=9,\ n_2=0,\ m=0\rangle$ parabolic state by a rectangular HCP. For a fixed value of N_{max}, the calculated ionization probability as a function of the Sturmian parameter exhibits a characteristic plateau. Moreover, the size of the plateau increases for increasing values of N_{max}. This is precisely the behavior expected; i.e., if N_{max} is large enough, the calculation must be stable with respect to variations of the basis set. Therefore, the value of the plateau corresponds to a converged ionization probability. The results in Fig. 6 can be compared with the work of Schwartz [17] who undertook the first accurate time-independent calculations for e-H scattering employing a similar method. However, because of limited computing power available at that time, the plateaus

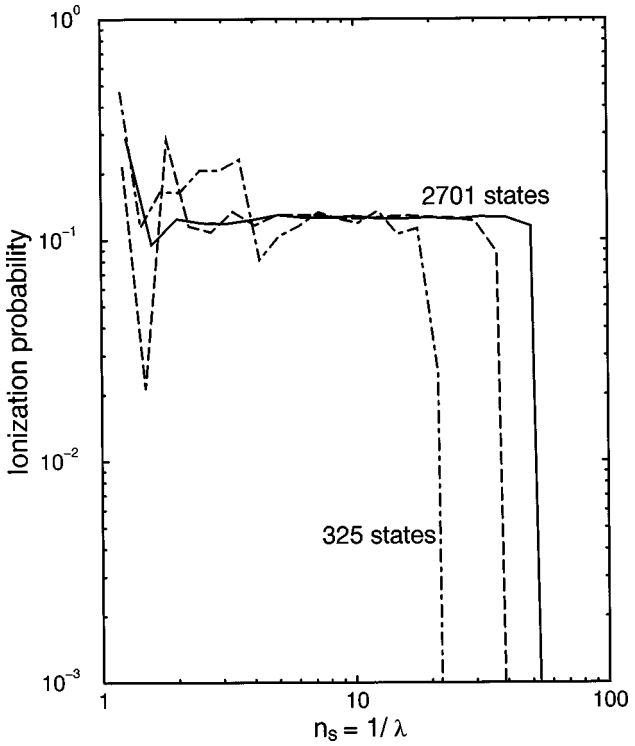

FIG. 6. Ionization probability of H($n_1=9,\ n_2=0,\ m=0$) subject to a rectangular HCP with $F_0=0.3$ and $T_0=0.5$ as a function of $n_s=\lambda^{-1}$. The various curves in the figure correspond to basis sizes of $N_{max}=325,1035,2701$. The larger the basis, the broader the stabilization plateau.

appeared as shallow minima. The stabilization method can not only provide accurate results, but also furnish a tool that can be used to learn how to choose the most appropriate Sturmian parameter. The stabilization plateau starts to develop at $n_s \lesssim 10$ even for a small basis size. This is partly due to the fact that a basis set with $n_s \simeq 10$ can provide a very good representation of the initial electronic state. However, for the finite subspace to cover the entire time development of the wave function it must also be able to provide a good description of the intermediate and final states. As discussed above, the smaller n_s, the better the representation of continuum states. This is the reason why the optimum Sturmian parameter is slightly smaller than 10.

Whether or not an accurate calculation of the ionization can be performed depends on both the duration and the strength of the HCP. Clearly, for large enough values of T_p or F_p the exact wave function can spread out into regions of coordinate and momentum space that are not properly described by a finite basis set. This is illustrated in Fig. 7, which shows the time evolution of the probability density associated with finding the electron with a given energy E;

$$\frac{dP}{dE}(E)=(\delta E)^{-1}\sum_{E-(\delta E/2)\le E_k\le E+(\delta E/2)}|\langle\phi_k^{\lambda}|\Psi(T)\rangle|^2, \tag{26}$$

where δE is a fixed energy interval. The figure is displayed in scaled units and, therefore, at $t=0$ the energy distribution peaks at $E_0=-2n_i^2E=-1$. For longer times, the probability distribution spreads out in energy, much like a wave packet.

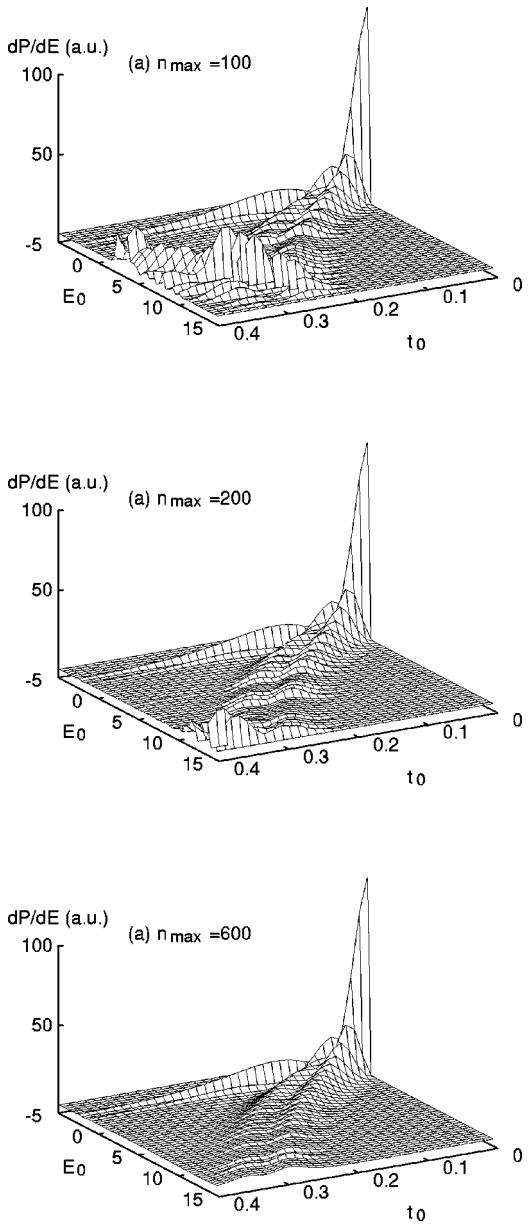

FIG. 7. Time evolution of the probability density for finding the electron with a given scaled energy E_0. The initial electronic state is $n=5$, $m=0$, $n_2=0$ (i.e., a downhill Stark state). The calculations were performed using $n_s=3$ and a restricted basis set of $n_2=0$ downhill Sturmian states and, therefore, $n_{max}=N_{max}$ for this case. The quasi-one-dimensional (1D) atom is subject to a rectangular pulse with $F_0=4$ and a variable duration T_0. The basis-set sizes are (a) $n_{max}=100$, (b) $n_{max}=200$, and (c) $n_{max}=500$.

Eventually, the wave packet is reflected [Fig. 7(a)] as it reaches a region beyond the effective range that is properly described by the basis. Figures 7(b) and 7(c) show that for increasing basis size the reflection occurs at later times and eventually disappears.

Using the present approach employing up to 4000 basis states and restricting the ionization probabilities to less than 15%, stabilization can be typically found for scaled durations $T_0 \lesssim 3$. Figure 8 illustrates this practical limit for the calculation of the scaled momentum transfers necessary to ionize 10% of Rydberg hydrogen atoms in the extreme parabolic states. Because both extreme parabolic states within a given

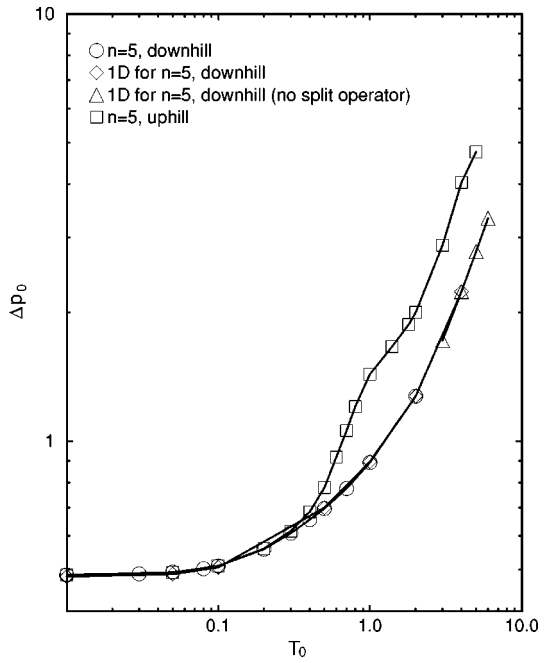

FIG. 8. Scaled momentum transfer for 10% ionization threshold of hydrogen atoms in various parabolic states as function of the scaled pulse duration for rectangular pulses. Also included for initial ($n_2=0$) downhill states are results obtained using a quasi-one-dimensional (1D) basis set of only downhill Sturmian states calculated with and without the split operator method.

n manifold possess identical momentum distributions, the ionization thresholds agree with each other in the limit of ultrashort HCPs ($T_0 \ll 1$). For pulses with a finite duration, ''downhill'' ($n_2=0$, or redshifted) parabolic states are more easily ionized than ''uphill'' ($n_1=0$, or blueshifted) states since their corresponding wave functions are localized near the top of the potential barrier generated by the pulse. This is the reason why the static field ionization threshold for hydrogenic downhill states is smaller than that for uphill states that are localized near the repulsive potential wall (see, e.g., [23]). For the same reason, fully converged calculations for uphill states can be carried out for longer times (i.e., ionized electrons from a downhill state reach the boundaries of the basis set more rapidly). Figure 8 also shows, however, that calculations for extreme downhill states can be extended using a restricted basis set of extreme downhill Sturmian states; i.e., a quasi-one-dimensional (1D) calculation. This indicates that the electronic dynamics leading to ionization develops in a quasi-one-dimensional space along the reaction coordinate across the saddle, the parabolic coordinate $\eta=r-z$ [8]. All of the results in the following section are fully converged according to the stabilization criteria discussed above.

IV. RESULTS AND DISCUSSION

In the limit of ultrashort HCPs, the results of our finite basis-set expansion can be tested against exact calculations. That is, matrix elements of the evolution operator in this limit [Eq. (6)] are given by well-known inelastic form factors (see, e.g., [24]). Figures 9 and 10 display a comparison of the results of our finite basis-set calculation with exact calculations for the spectrum of energy states that become populated

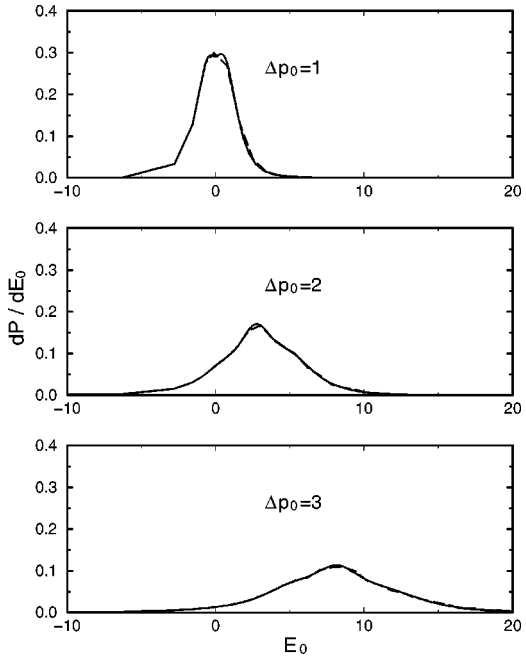

FIG. 9. Distribution of final energy states resulting from the interaction of an ultrashort HCP of various strengths with a hydrogen atom in the initial parabolic state $n=5,\ n_1=0,\ m=0$: exact results (thick curve); finite basis-set expansion with $n_{max}=65\ n_s=3$ (thin curve).

by a HCP [Eq. (26)]. The exact calculation for continuum states ($E=K^2/2>0$) is given by

$$\frac{dP^{USP}}{dE}=K\int d\Omega\left|\langle\psi_{\boldsymbol{K}}^{-}|e^{i\Delta p\ z}|\varphi_i\rangle\right|^2, \tag{27}$$

where $\psi_{\boldsymbol{K}}^{-}$ is an incoming continuum Coulomb state with

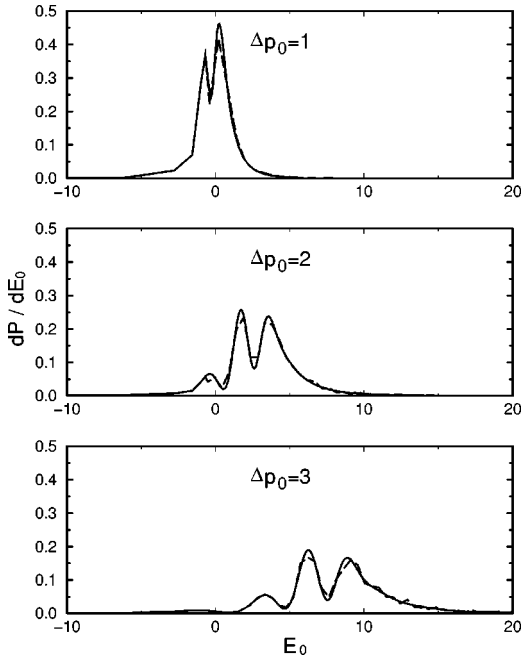

FIG. 10. Distribution of final energy states resulting from the interaction of an ultrashort HCP of various strengths with a hydrogen atom in the initial spherical state $n=5,\ l=1,\ m=0$: exact results (thick curve); finite basis-set expansion with $n_{max}=65\ n_s=3$ (thin curve).

wave number $\boldsymbol{K}$ ($E=K^2/2$). Due to Coulomb threshold laws for the population of near-threshold states ($E\simeq 0$), in the limit $E\rightarrow 0$, Eq. (27) should tend to the corresponding result for bound states, $E=-Z^2/(2n^2)<0$, which is given by

$$\frac{dP^{USP}}{dE}=\frac{n^3}{Z^2}\sum_{l,m}\left|\langle n,l,m|e^{i\Delta p\ z}|\varphi_i\rangle\right|^2. \tag{28}$$

Figures 9 and 10 show that the results obtained using a finite basis expansion are in very good agreement with the exact calculations. The marked differences between the energy distributions for an extreme parabolic state and a spherical state can be traced back to differences in their initial momentum distributions along the direction of the pulse. That is, the electronic wave function, immediately after application of an ultrashort HCP, corresponds to the initial state shifted in momentum space by $\Delta\boldsymbol{p}$. Therefore, Figs. 9 and 10 roughly correspond to the averaged projection of a shifted momentum distribution onto the z axis (i.e., the Compton profile). The oscillatory behavior of the energy distributions for an initial $n=5,\ l=1,\ m=0$ state is related to the nodal structure of the initial momentum distribution and is not present in classical simulations. The structureless spectrum of the initial parabolic state ($n=5,\ n_1=0,\ m=0$) is a direct reflection of the fact that the momentum space probability density [25] of extreme parabolic states is node free. The momentum wave function of a parabolic state is given by

$$\langle\boldsymbol{p}|n_1,n_2,m\rangle\propto\left(\frac{2p_0^2}{p^2+p_0^2}\right)^2 \times d^{(n-1)/2}_{(n_2-n_1+m)/2,(n_1-n_2+m)/2}(2\xi)e^{im\phi_p}, \tag{29}$$

where p,θ_p,φ_p are spherical coordinates in momentum space, $p_0=Z/n$, $\xi=\cos^{-1}[2pp_0/(p^2+p_0^2)\sin\theta_p]$, and $d^i_{j,k}$ is a matrix element of a finite rotation. For $m=0$ extreme parabolic states

$$\begin{aligned} d^{(n-1)/2}_{\pm(n-1)/2,\mp(n-1)/2}(2\xi)&=d^{(n-1)/2}_{\mp(n-1)/2,\pm(n-1)/2}(-2\xi)\\ &\propto\left(\frac{p_0^4+p^4+2p_0^2p^2\cos^2\theta_p}{(p_0^2+p^2)^2}\right)^{n-1}\\ &=\left(\frac{p_0^4+p^4+2p_0^2p_z^2}{(p_0^2+p^2)^2}\right)^{n-1}, \end{aligned} \tag{30}$$

and, therefore, $|\langle\boldsymbol{p}|n_1,n_2,m\rangle|^2$ is node free.

The position of the absolute maximum of the final-state energy distribution for a given large Δp can be understood from the fact that the expectation value of the energy after an ultrashort HCP is given by

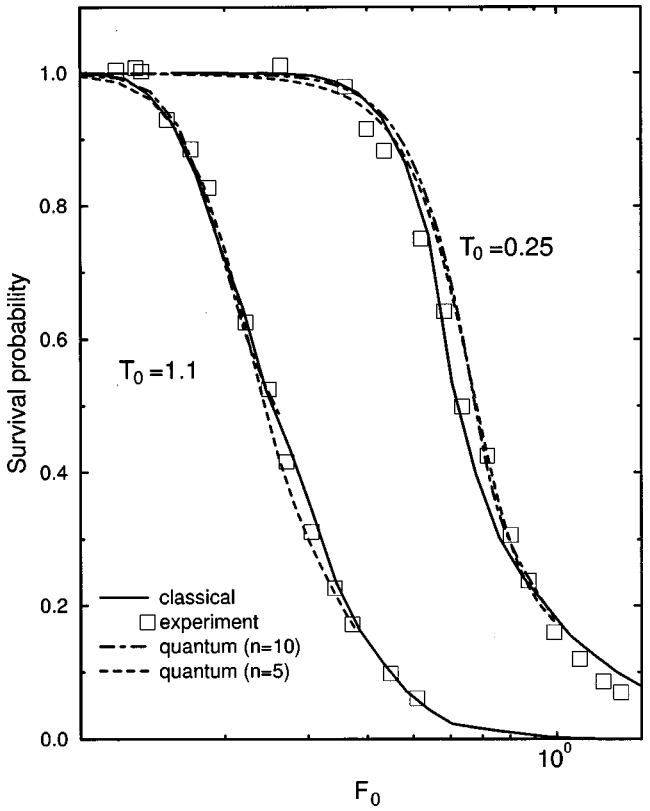

FIG. 11. Survival probability as a function of the scaled peak field for two effective pulse durations. Quantum calculations using rectangular pulses for H($n=10$, $l=1$) and H($n=5$, $l=1$) are compared with experimental data and classical calculations [3] for the K(388p) atom. The classical calculations use the experimentally determined pulse shapes that feature a very fast rise time.

$$\langle E\rangle=\langle e^{i\Delta pz}\varphi_i|H_{at}|e^{i\Delta pz}\varphi_i\rangle$$

$$=\langle\varphi_i|H_{at}|\varphi_i\rangle+\frac{(\Delta p)^2}{2}+\Delta p\langle\varphi_i|p_z|\varphi_i\rangle \qquad (31)$$

$$=E_{n_i}+\frac{(\Delta p)^2}{2}, \qquad (32)$$

or, equivalently, $\langle E_0\rangle=-1+(\Delta p_0)^2$. The energy distributions in Figs. 9 and 10 are seen to peak at approximately this energy. The peak is a direct manifestation of the Bethe ridge in atomic collision physics [26].

Figure 11 shows that structures in the energy spectrum of the ejected electrons are not always evident in the total survival probability

$$P_{sur}=1-P_{ion}=1-\int_0^\infty dE\,\frac{dP}{dE} \qquad (33)$$

as a function of the peak field. In scaled units, quantum results for $n_i=5$ and $n_i=10$ are in very good agreement with each other, illustrating that the scaling invariant limit is already reached using only moderately high quantum levels (departures from scaling invariance are only expected to occur for very small ionization probabilities [6]). The quantum calculations (for rectangular pulses) are in good agreement with classical calculations and experimental data for $n_i=388$ obtained using HCPs with a very short rise time.

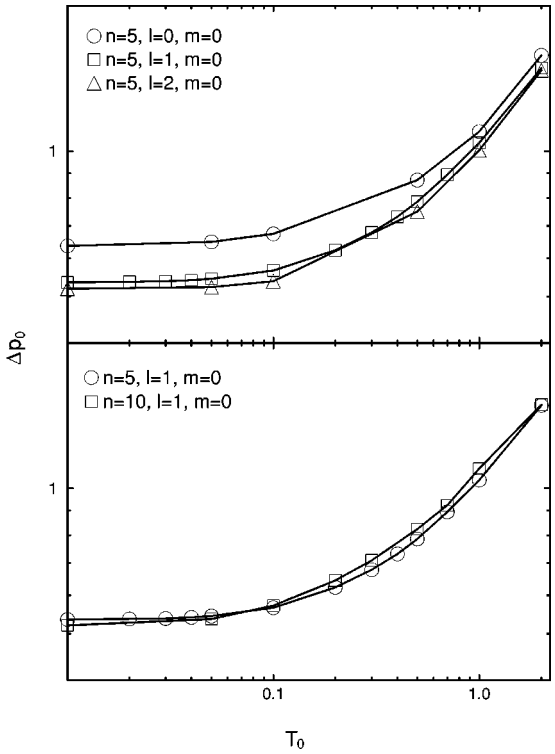

FIG. 12. Scaled momentum transfer for 10% ionization of hydrogen atoms in various spherical states as a function of the scaled pulse duration for rectangular pulses. The values of n used in these quantum calculations are as indicated.

In view of the very good agreement between our quantum calculations and our previously published measurements and classical results, the disagreement recently reported by Kristensen *et al.* [4] for pulse durations $T_0>2$ is surprising. In the following we analyze three possibilities that may influ-

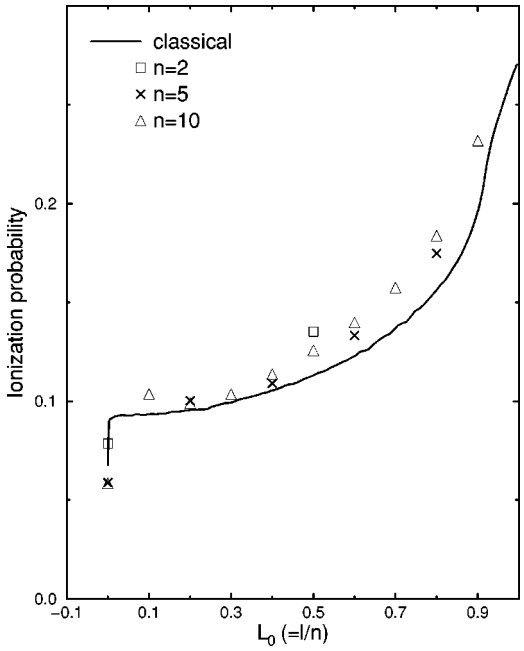

FIG. 13. Ionization probability of $m=0$ states produced by an ultrashort HCP with $\Delta p_0=0.54$ as a function of the scaled angular momentum. The values of n used in the quantum calculations are as indicated.

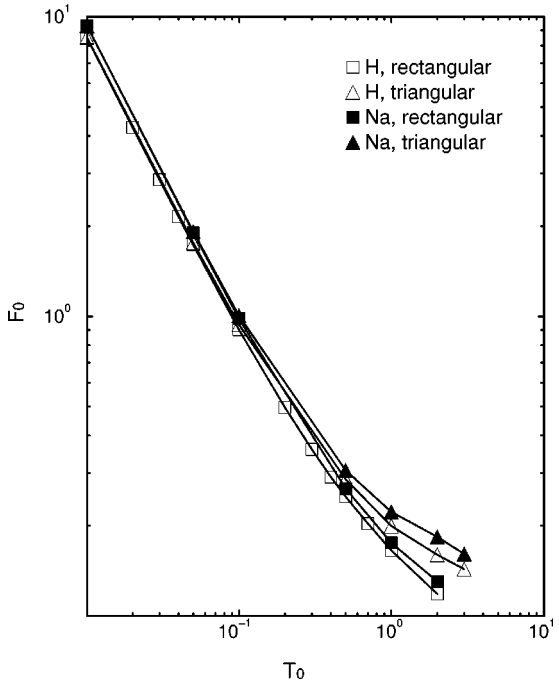

FIG. 14. Scaled peak field for 10% ionization threshold of H($n=5$, $l=1$, $m=0$) and Na($n=5$, $l=1$, $m=0$) atoms as a function of the scaled pulse duration for rectangular and triangular pulses.

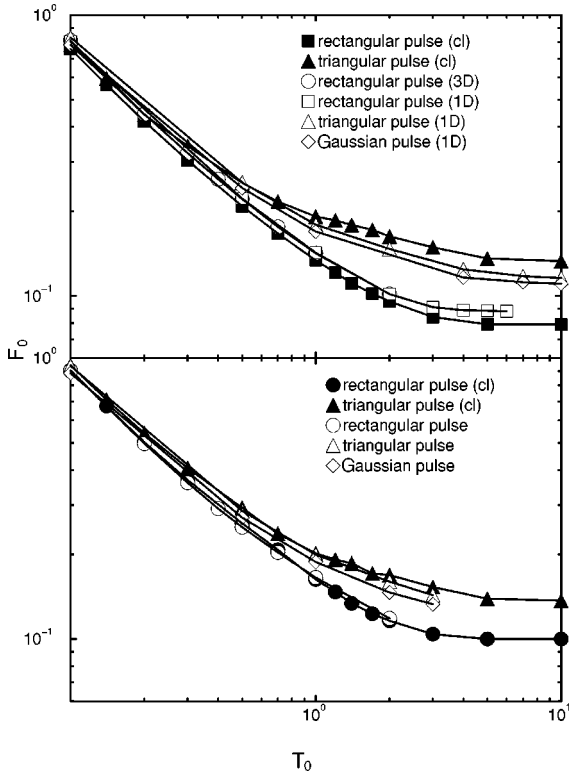

FIG. 15. Scaled peak field for 10% ionization of (a) H($n=5$, $n_2=0$, $m=0$) and (b) H($n=5, l=1, m=0$) calculated classically (cl) and quantum mechanically (qm) as a function of the scaled pulse duration for various pulse shapes (see text).

ence the ionization thresholds: (i) the statistical combination of $l=0$ (25%) and $l=2$ (75%) initial states in the experiments, (ii) core effects, and (iii) the actual shape of the experimental pulses.

Figure 12 displays the scaled momentum transfer required to produce 10% ionization of hydrogen atoms in states with various well-defined initial angular momenta. Clear differences in the thresholds for different states are observed for short pulses. Figure 13 shows that the quantum ionization probability, as a function of $L_0=l/n$, is scaling invariant for increasing n value and, moreover, that it agrees with the classical predictions. For $m=0$ there exists a sharp discontinuity between the results for $l=0$ and $l=1$, which can be easily understood geometrically from the differences in the projection of the momentum distributions for s and p ($m=0$) states along the z axis. In fact, the results for $l=0$ coincide with the statistical average over $m=0,\pm1,\pm2$ of $l=2$ states (not shown). Note, however, that the difference between $l=0$ and $l=2$ states cannot even partly explain the discrepancies between theory and the experiment of Kristensen *et al.* [4], since the largest differences between different states occur in the ultrashort pulse limit. For long duration HCPs the angular momentum rapidly increases due to Stark precession around the electric field.

Figure 14 illustrates the effect of a finite-size core on the ionization thresholds. The calculations were performed for Na($5p$) states, which should overemphasize the core effects to be expected for higher n levels. Clearly, core effects play only a minor role in determining the ionization threshold, the difference being on the order of the experimental uncertainties. This agrees with the experimental observation of Kristensen *et al.* [4] that the ionization thresholds for alkali-metal atoms with quite different quantum defects (Li, Rb) are in very good agreement with each other.

The data of Kristensen *et al.* [4] were obtained using HCPs with a long rise time. One may therefore suspect that they cannot be properly modeled using rectangular pulses. This is illustrated in Fig. 15, where the results of classical and quantum calculations for rectangular, triangular, and Gaussian pulses [Eqs. (7)–(9)] are displayed. As expected, the results converge in the short pulse limit because the ionization probability depends solely on the integral of the pulse (i.e., the momentum transfer Δp). However, sizable differences exist for long pulses. Note that the differences are larger for the extreme downhill parabolic state than for a p (or d) state. The origin of this difference lies in the different degree of adiabaticity displayed by parabolic and spherical states. Since parabolic states diagonalize the Stark perturbation within a given shell, nonadiabatic effects require dynamical coupling to different shells. For $T_0>1$, i.e., when the rise time is large compared to the orbital period, extreme parabolic states evolve approximately adiabatically, because of the absence of a large number of avoided crossings, which leads to an increased stability against ionization. Spherical states, on the other hand, show much stronger nonadiabatic couplings for $T_0>1$ due to both intrashell l mixing and coupling to other manifolds. In contrast, HCPs with a sudden turn-on dynamically couple the initial Stark state to other n levels, which can be ionized more easily than the adiabatically shifted state.

Classically, the ratio of rise time to orbital period provides the criterion for the adiabaticity of the evolution. If this ratio

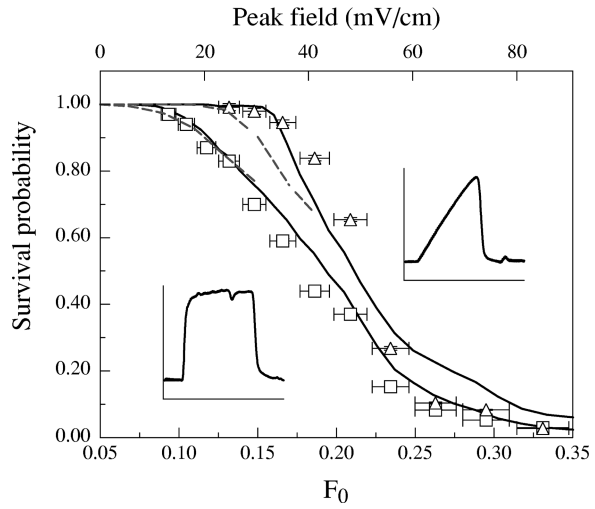

FIG. 16. Survival probability of K(388p) atoms as a function of the scaled peak field (lower axis) or peak field in mV/cm (upper axis): experimental data (open squares and open triangles); classical calculations for K(388p) atoms (solid lines); and quantum calculations for H(5p) states scaled to H(388p) (dashed lines). The insets show the experimentally determined rectangular and triangular pulse profiles that have FWHM durations of $\sim$29 ns ($T_0=3.3$) and 31 ns ($T_0=3.5$), respectively. The survival probabilities on the right (left) are associated with the triangular (rectangular) pulse. Both measurements and calculations correspond to a statistical distribution of m substates.

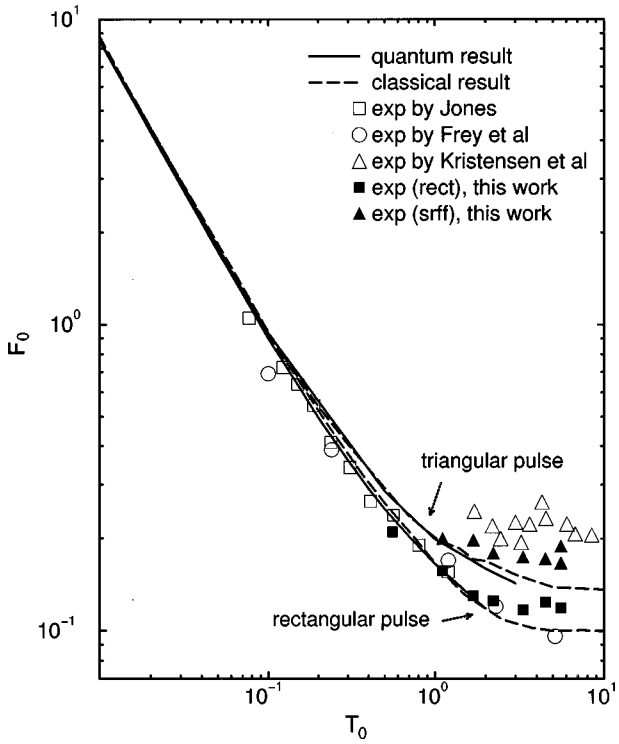

FIG. 17. Scaled peak field for 10% ionization of hydrogen np atoms as a function of the scaled pulse duration. The theoretical calculations for rectangular and triangular pulses are compared with the present measurements using pulses with a fast rise time (rect) or a slow rise time (srff), as well as with the data of Jones *et al.*, scaled by a factor of 2.5 [1], Frey *et al.* [3], and Kristensen *et al.* [4].

is large, the unperturbed Kepler orbit evolves adiabatically into a field perturbed orbit. The classical sudden limit, on the other hand, is characterized by the dependence of the energy of the perturbed orbit on the local position of the electron at the time of the turn-on of the field. On the quantum level, there exists an additional time scale in terms of the ratio of the nonadiabatic coupling strength to the size of the avoided crossings through which the evolution from the zero-field energy levels to the high-field levels proceeds. To the extent that these avoided crossings are isolated and the coupling involves only few states, this is an intrinsically nonclassical process. The fact that hydrogen and alkali-metal atoms display the same rise-time dependence indicates that the narrow avoided crossings between different Stark states due to the nonhydrogenic core in the alkali-metal atoms do not play a significant role. They are traversed completely diabatically. Hydrogen displays a different type of avoided crossing, sometimes termed ''hidden'' crossing [27]. It corresponds to an interaction between the most redshifted Stark states of adjacent manifolds and is characterized by a width that is a considerable fraction of the zero-field level spacing. Translated into classical dynamics, this amounts to a time scale of a few zero-field orbital periods. The avoided crossing occurs above the field ionization threshold in the region of overlapping resonances [28]. The observed rise-time dependence is related to the inverse level density of resonances near and above the ionization threshold.

In order to corroborate the theoretical predictions, we have performed a series of measurements using apparatus and techniques described elsewhere. In the experiments, ionization of K(np) Rydberg atoms with ($n\sim388$) was investigated using pulses having essentially the same peak amplitude and full width at half maximum but different pulse shapes, i.e., different rise and fall times. Results obtained using the extremes of these pulse shapes, namely a nearly rectangular pulse with a fast rise time and a ''chirped'' pulse with a slow rise time and fast fall (srff) are presented in Fig. 16, which shows the measured survival probability as a function of the peak amplitude of the pulse for a relatively long pulse, $T_0\simeq3$. For reference, the experimentally determined pulse profiles are included in the figure as insets. The data show that, indeed, the survival probability is quite sensitive to the rise time and that the ionization threshold increases for increasing rise time. Figure 16 also includes the results of quantum and classical calculations undertaken using the experimental pulse profiles. Quantum calculations for H(5p) exhibit a similar, but slightly reduced, shift of the ionization threshold. Because the measurements were performed for K(388p), the differences in the shift possibly provide an indication that the scaling invariant limit ($n\rightarrow\infty$) has not yet been reached for $n=5$. Unfortunately we have been unable to obtain converged quantum calculations for $n>5$ levels with these long pulses. However, classical calculations for K(388p) atoms are found to be in good agreement with the measurements.

In Fig. 17 we compare our quantum and classical thresholds for 10% ionization by rectangular and triangular pulses acting on hydrogen atoms with the present experimental measurements and previously published data. Note that the experimental profiles do not exactly agree with the theoretical pulse shapes. Clearly, the dependence of the ionization thresholds on the rise time explains, at least in part, the disagreement between the data of Kristensen *et al.* [4] and clas-

sical calculations for rectangular pulses. The measurements of Frey *et al.* [3] agree with these calculations because the experimental pulses in this case featured a short rise time that was smaller than the orbital period of the Rydberg atoms and that approximated the rectangular shape quite well. The present measurements using pulse profiles with a long rise time are indeed much closer to the data of Kristensen *et al.* For short pulses, the calculations are seen to be in good agreement with the data of Frey *et al.* [3] and the normalized data of Jones *et al.* [1]. The differences between classical and quantum calculations for the entire range of pulse durations are found to be much smaller than typical experimental uncertainties.

V. CONCLUDING REMARKS

We have described in detail a quantum-mechanical coupled-channels approach to study the ionization of atoms by half-cycle pulses. We have shown that the accuracy of the calculations can be established using the stabilization method. Presently, our calculations are limited to short durations ($T_0 \lesssim 4$). Work is underway to extend these to longer pulses using a nonunitary representation of the evolution operator.

We have shown that quantum calculations are scaling invariant and are in very good agreement with classical calculations even for levels with relatively low principal quantum numbers. Moreover, we have presented independent experimental data that are also in very good agreement with the calculations. Thus, the disagreement recently reported by Kristensen *et al.* [4] between classical calculations and experiment is largely due to the shape of these pulses. In particular, we have shown that when the duration of the pulse is longer than the orbital period of the atom, the ionization thresholds become sensitive to the rise time of the electric field.

ACKNOWLEDGMENTS

Support for this work has been provided by the U.S. Department of Energy, Office of Basic Energy Sciences, Division of Chemical Sciences, under Contract No. DE-AC05-96OR22464 with ORNL, managed by Lockheed Martin Energy Research Corporation, by the NSF, and by the Robert A. Welch Foundation.

APPENDIX: THE CLASSICAL LIMIT

In the classical limit, the time evolution of the electronic wave function is modeled using an ensemble of classical particles that mimic the initial quantum state. That is, the quantum wave function $\Psi(\boldsymbol{r},t)$ is replaced by a classical probability density in phase space $f(\boldsymbol{r},\boldsymbol{p},t)$. Formally, the time evolution of this density is governed by the classical Liouville equation for the Hamiltonian $H(t)$ in Eq. (1),

$$\frac{\partial f}{\partial t} = [H, f], \tag{A1}$$

with the boundary condition

$$f(\boldsymbol{r},\boldsymbol{p},t) \underset{t\to 0}{\rightarrow} f_i(\boldsymbol{r},\boldsymbol{p}), \tag{A2}$$

where $[,]$ denotes a Poisson bracket and f_i is the initial state. Since phase-space points evolve in time independently, the Liouville equation can be easily solved using a Monte Carlo technique. The resulting method is usually referred to as the classical trajectory Monte Carlo approach [11].

There exists no unique way of determining the initial phase-space state so that it mimics the initial quantum state. The most common choice of initial conditions, which we adopt here, is a subset of a microcanonical ensemble,

$$f_i(\boldsymbol{r},\boldsymbol{p}) = C_i \delta\left[E_i - \frac{p^2}{2} - V_{at}(r)\right] \upsilon_i, \tag{A3}$$

where C_i is normalization constant, E_i is the initial quantum-mechanical binding energy, and υ_i is a characteristic function representing the other quantum numbers of the initial state. This type of initial state yields the exact quantum-mechanical probability density of the momentum for a statistical average of states within a given n manifold.

For a hydrogenic initial spherical state $|n_i, l_i, m\rangle$,

$$\upsilon_{l_i,m_i} = \Theta(L - l_i)\Theta(l_i + 1 - L)\Theta\left(L_z - \frac{L(2m_i - 1)}{2l_i + 1}\right) \times \Theta\left(\frac{L(2m_i + 1)}{2l_i + 1} - L_z\right), \tag{A4}$$

where $\boldsymbol{L} = \boldsymbol{r} \times \boldsymbol{p}$ is the classical angular momentum and Θ denotes a step function. In turn, for a hydrogenic parabolic state with quantum numbers n_i, n_{1i}, n_{2i}, we use

$$\upsilon_{n_{1i},n_{2i}} = \Theta(N_1^c - n_{1i} + \tfrac{1}{2})\Theta(-N_1^c + n_{1i} - \tfrac{1}{2}) \times \Theta(N_2^c - n_{2i} + \tfrac{1}{2})\Theta(-N_2^c + n_{2i} - \tfrac{1}{2}), \tag{A5}$$

$$N_{1,2}^c = \tfrac{1}{2}[n_i\,(1 \mp A_z) - (|L_z| + 1)], \tag{A6}$$

where $\boldsymbol{A} = \boldsymbol{p} \times \boldsymbol{L} - \hat{\boldsymbol{r}}$ is the Runge-Lenz vector.

[1] R. R. Jones, D. You, and P. H. Bucksbaum, Phys. Rev. Lett. **70**, 1236 (1993).

[2] R. R. Jones, N. E. Tielking, D. You, C. Raman, and P. H. Bucksbaum, Phys. Rev. A **51**, R2687 (1995); N. E. Tielking, T. J. Bensky, and R. R. Jones, *ibid.* **51**, 3370 (1995); N. E. Tielking and R. R. Jones, *ibid.* **52**, 1371 (1995).

[3] M. T. Frey, F. B. Dunning, C. O. Reinhold, and J. Burgdörfer, Phys. Rev. A **53**, R2929 (1996).

[4] P. Kristensen, G. M. Lankhuijzen, and L. D. Noordam, J. Phys. B **30**, 1481 (1997); G. M. Lankhuijzen and L. D. Noordam, Phys. Rev. Lett. **74**, 355 (1995).

[5] C. W. S. Conover and J. H. Rentz, Phys. Rev. A **55**, 3787 (1997).

[6] C. O. Reinhold, M. Melles, H. Shao, and J. Burgdörfer, J.

Phys. B **26**, L659 (1993); **29**, 377 (1996); C. O. Reinhold, M. Melles, and J. Burgdörfer, Phys. Rev. Lett. **70**, 4026 (1993).

[7] C. O. Reinhold, H. Shao, and J. Burgdörfer, J. Phys. B **27**, L469 (1994).

[8] C. O. Reinhold, J. Burgdörfer, R. R. Jones, C. Raman, and P. H. Bucksbaum, J. Phys. B **28**, L457 (1995); C. O. Reinhold and J. Burgdörfer, Phys. Rev. A **51**, R3410 (1995).

[9] A. Bugacov, B. Piraux, M. Pont, and R. Shakeshaft, Phys. Rev. A **51**, 4877 (1995); **51**, 1490 (1995).

[10] P. Krstic and Y. Hahn, Phys. Rev. A **50**, 4629 (1994); R. Gebarowski, J. Phys. B **30**, 2143 (1997); C. D. Schwieters and J. B. Delos, Phys. Rev. A **51**, 1023 (1995); K. J. LaGattuta and P. Lerner, *ibid.* **49**, R1547 (1994); V. Enss, V. Kostrykin, and R. Schrader, *ibid.* **50**, 1578 (1994); T. F. Jiang and C. D. Lin, *ibid.* **55**, 2172 (1997); F. Robicheaux, *ibid.* **56**, R3358 (1997).

[11] R. Abrines and I. C. Percival, Proc. Phys. Soc. London **88**, 861 (1966); **88**, 873 (1966); I. C. Percival and D. Richards, Adv. At., Mol., Opt. Phys. **11**, 1 (1975); R. E. Olson, Phys. Rev. A **24**, 1726 (1981).

[12] R. R. Jones, Phys. Rev. Lett. **76**, 3927 (1996).

[13] C. O. Reinhold, J. Burgdörfer, M. T. Frey, and F. B. Dunning, Phys. Rev. A **54**, R33 (1996).

[14] M. T. Frey, F. B. Dunning, C. O. Reinhold, and J. Burgdörfer, Phys. Rev. A **55**, R865 (1997).

[15] L. D. Landau and E. M. Lifshitz, *Mechanics* (Pergamon, Oxford, 1960).

[16] A. U. Hazi and H. S. Taylor, Phys. Rev. A **1**, 1109 (1970); V. A. Mandelshtam, T. R. Ravuri, and H. S. Taylor, Phys. Rev. Lett. **70**, 1932 (1993); J. Müller, X. Yang, and J. Burgdörfer, Phys. Rev. A **49**, 2470 (1994).

[17] C. Schwartz, Phys. Rev. **124**, 1468 (1961).

[18] M. Rotenberg, Ann. Phys. (N.Y.) **19**, 262 (1962); Adv. At. Mol. Phys. **6**, 233 (1970).

[19] R. Shakeshaft, Phys. Rev. A **18**, 1930 (1978); **14**, 1626 (1976).

[20] M. Pont, D. Proulx, and R. Shakeshaft, Phys. Rev. A **44**, 4486 (1991).

[21] A. Maquet, S. Chu, and W. P. Reinhart, Phys. Rev. A **27**, 2946 (1983).

[22] M. D. Feit, J. A. Fleck, and A. Steiger, J. Comp. Physiol. **47**, 412 (1982).

[23] T. F. Gallagher, Rep. Prog. Phys. **51**, 143 (1988).

[24] Dž. Belkić, J. Phys. B **14**, 1907 (1981).

[25] M. J. Englefield, *Group Theory and the Coulomb Problem* (John Wiley & Sons, Inc., New York, 1972).

[26] M. Inokuti, Rev. Mod. Phys. **43**, 297 (1971); C. O. Reinhold and J. Burgdörfer, J. Phys. B **26**, 3101 (1993).

[27] E. A. Solov'ev, Sov. Phys. JETP **54**, 893 (1981); T. P. Grozdanov and E. A. Solov'ev, Phys. Rev. A **42**, 2703 (1990).

[28] J. Burgdörfer, X. Z. Yang, and J. Müller, Chaos Solitons Fractals **5**, 1235 (1995).